# In-plane canted ferromagnetism, intrinsic Weyl fermions, and large anomalous Hall effect in the kagome semimetal $Rh_3Sn_2S_2$

Meng-Xin Wu,[1,*] Yu-Hao Wei,[1,*] Da-Shuai Ma,[2,3,†] Peng Wang,[1] Nan Gao,[4] Shao-Yi Wu,[5,‡] and Min-Quan Kuang[1,§]

[1]*Chongqing Key Laboratory of Micro & Nano Structure Optoelectronics and School of Physical Science and Technology, Southwest University, Chongqing 400715, People's Republic of China*

[2]*Institute for Structure and Function, Department of Physics, and Chongqing Key Laboratory for Strongly Coupled Physics, Chongqing University, Chongqing 400044, People's Republic of China*

[3]*Center of Quantum Materials and Devices, Chongqing University, Chongqing 400044, People's Republic of China*

[4]*School of Material Science and Engineering, Taizhou University, Taizhou 318000, People's Republic of China*

[5]*Department of Applied Physics, School of Physics, University of Electronic Science and Technology of China, Chengdu 611731, People's Republic of China*

(Received 11 September 2023; revised 27 October 2023; accepted 7 November 2023; published 20 November 2023)

Magnetic Weyl semimetals can reveal a renowned electronic transport phenomenon, i.e., the anomalous Hall effect due to the intrinsic Berry curvature promoted by the Weyl fermions. Here, the layered kagome compound $Rh_3Sn_2S_2$ is identified as a ferromagnetic Weyl semimetal by first-principles calculations. When the spin-orbit coupling is absent, three sets of nontrivial Weyl nodal lines emerge in the spin-up channel, while the spin-down bands are fully gapped. The obtained magnetocrystalline anisotropy energy indicates that $Rh_3Sn_2S_2$ has an in-plane canted magnetic order with a 30° angle to the *a* axis. As a consequence, the spin-orbit coupling breaks the time-reversal symmetry, and the broken Weyl nodal lines give birth to one pair of Weyl points near the Fermi level. The chiral Weyl nodes, protected by the space inversion and the $C_{3z}$-rotation symmetry, act as the monopole source and sink of the Berry curvature and boost a large anomalous Hall conductivity approaching $580\ \Omega^{-1}\,\mathrm{cm}^{-1}$. This work unveils the magnetic, electronic, and topological properties as well as the anomalous Hall effect of $Rh_3Sn_2S_2$, which will facilitate future research on the unexplored topological phenomena in $Rh_3Sn_2S_2$.

DOI: 10.1103/PhysRevB.108.174430

## I. INTRODUCTION

Kagome materials consisting of corner-sharing triangles have attracted much interest due to their fertile electronic and topological properties [1–20]. One of the most intriguing features is the anomalous Hall effect (AHE) [21,22], which usually accompanies the time-reversal symmetry (TRS) breaking. As an important electronic transport phenomenon, the emergent AHE can be driven by an external magnetic field [23,24] or be introduced by the intrinsic magnetic or charge order. Referring to the source of the intrinsic AHE, the widely accepted scenarios are the Berry curvature of the occupied Bloch bands [25], the topological orbital moment originating from the spin chirality [22,26–28], and the charge order stemming from the charge density wave (CDW) [29,30]. Moreover, these factors might entangle with each other and can be further tuned by the strain [31,32], pressure [33,34], magnetic order [35,36], and element substitution [37–42], which paves the way for potential applications in spintronics.

In addition, recent work reveals that the anomalous Hall conductivity (AHC) varies from dozens to thousands of S/cm for kagome magnets, in which the magnetism arises from the transition metals Mn [22,43–46], Fe [2,46], and Co [47,48] or the rare-earth metals (Nd [49,50], Gd [41,44], Tb [41,51,52], Dy [40,41], Ho [40,41], Er [41,53], and U [35]). Noticeably, as for the kagome lattice, there might be an interplay between the geometric frustration, electronic correlation, and topological character, and hence kagome magnets provide a feasible playground to manipulate the AHE and then realize low-power-dissipation spintronics devices [46,54,55]. One notes that the mechanism of the AHE in rare-earth metal kagome magnets is obscure due to the complicated band structure from the strong spin-orbit coupling (SOC) and strong electron correlation [35,40,41,44,49–53], which increases the difficulty of manipulation and the threshold of application. Then, the remaining suitable candidates are transition metal kagome magnets, and one may ask whether there is any material with an intrinsic AHE where the kagome lattice and the magnetism come from a transition metal other than Mn, Fe, and Co. Here, we point out that $Rh_3Sn_2S_2$ is an ideal kagome Weyl semimetal with Rh atoms contributing the ferromagnetism and constructing the kagome lattice (Fig. 1).

Here, we propose $Rh_3Sn_2S_2$ as a kagome ferromagnetic Weyl semimetal (WSM) on the basis of first-principles calculations. The calculated magnetic moment without or with the SOC effect is 0.35 $\mu$B/Rh atom. The Curie temperature is estimated to be 61 K via the mean field theory (MFT) [56]. The calculated easy magnetization axis lies in the *ab* plane (Fig. 3).

*These authors contributed equally to this work.
†madason.xin@gmail.com
‡wushaoyi@uestc.edu.cn
§mqkuang@swu.edu.cn

 

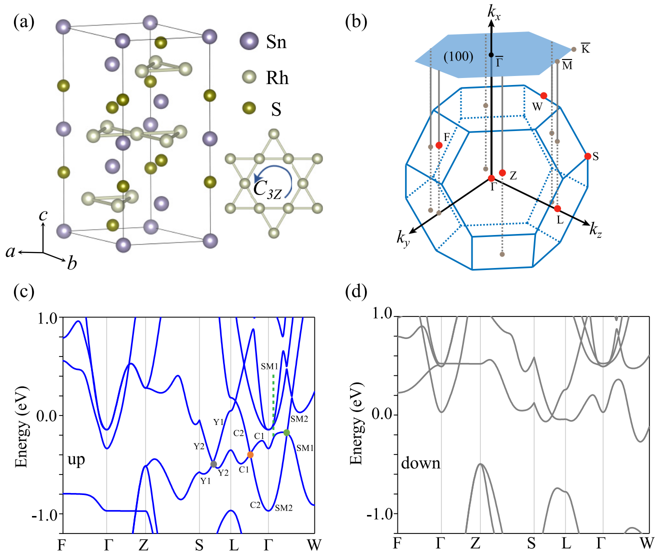


FIG. 1. Crystal and band structure without SOC. (a) Unit cell of $Rh_3Sn_2S_2$ where the Rh atoms constitute the kagome lattice with $C_{3z}$-rotation symmetry. (b) The first BZ with high-symmetry points and the projected (100) surface. (c) and (d) Band structure for the spin-up (c) and spin-down (d) directions. For the spin-up dispersion (c), the band crossing points are highlighted by the gray, orange, and green solid circles. The labels indicate the irreducible representations for the bands forming the band crossing points.

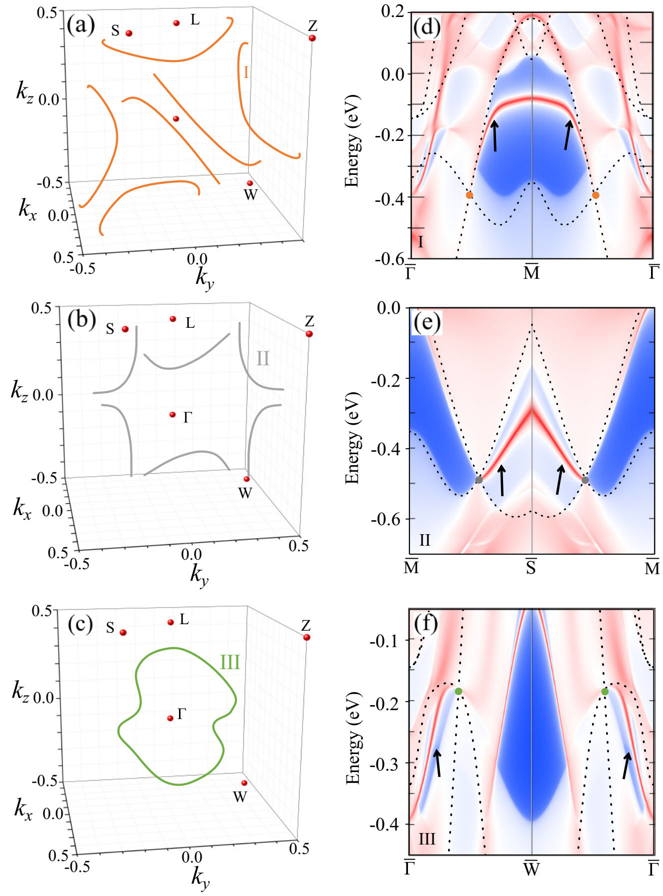


FIG. 2. Topological properties without SOC. (a)–(c) The WNLs in the first BZ (WNL-I, WNL-II, and WNL-III) echo the band crossings labeled in orange, gray, and green in Fig. 1(c), respectively. (d)–(f) The edge states calculated using WANNIERTOOLS [64] for WNL-I (d), WNL-II (e), and WNL-III (f) on the (100) surface, respectively. The dashed lines and solid arrows signify the band dispersion and the edge states, respectively.

With the SOC effect, the nontrivial Weyl nodal lines (WNLs) (Fig. 2) are broken, and six Weyl points (WPs) emerge near the Fermi level ($E_F$; Fig. 4). Moreover, the chiral WPs give birth to the intrinsic Berry curvature and bring in a large AHC approaching 580 $\Omega^{-1}\,\mathrm{cm}^{-1}$ (Fig. 4). When the magnetization direction rotates to the (0 0 1) direction, the AHC reaches 616 $\Omega^{-1}\,\mathrm{cm}^{-1}$. This work unlocks the magnetic, electronic, and topological features of $Rh_3Sn_2S_2$ and provides a veritable real kagome magnet to study the AHE and promising applications in the near future.

## II. COMPUTATIONAL METHODS

In this paper, the first-principles calculations were performed using the Vienna *ab initio* simulation package (VASP) in the framework of density functional theory (DFT) [57,58]. We adopted the strongly constrained and appropriately normed (SCAN) generalized gradient approximation (GGA) as the exchange-correlation functional [59–61]. The plane-wave truncation energy was selected as 500 eV, and the convergence accuracy of the self-consistent iteration was set as $1 \times 10^{-6}$ eV/atom. The force convergence criterion for structural relaxation is $-1 \times 10^{-2}$ eV/Å. The Brillouin zone (BZ) was sampled with a $14 \times 14 \times 14$ $k$ mesh for the structural optimization and self-consistent calculation. To better describe the electronic structures, the repulsive on-site Coulomb interaction $U$ for the Rh-3$d$ orbital was set to be 3.4 eV by matching the bands from the DFT+$U$ method to those of the Heyd-Scuseria-Ernzerhof (HSE) approach [62,63]. The Green's function iterative method implemented in the WANNIERTOOLS software package was adopted to demonstrate the surface electronic properties [64].

We first calculated the band structure of $Rh_3Sn_2S_2$ using the Perdew-Burke-Ernzerhof (PBE) method [59,65], and a flat band emerged near the Fermi level (Fig. S1 of the Supplemental Material (SM) [66]), suggesting a magnetic instability [4,67,68]. Then we performed the total energy calculation for the primitive cell using the HSE approach [62,63], and the ferromagnetic (FM) state had a lower energy (134.4 meV) than the nonmagnetic (NM) state, implying potential magnetism in $Rh_3Sn_2S_2$. To describe the possible strong on-site Coulomb interaction, the PBE+$U$ [69] method and the SCAN+$U$ [70,71] method were both introduced to calculate the band structure, and the test results indicated that the bands from the SCAN+$U$ method with a 3.4-eV repulsive on-site Coulomb interaction agreed well with the band dispersion from the HSE calculation (Fig. S2 [66]). Then, the SCAN+$U$ ($U = 3.4$ eV) method was adopted for all the calculations in the main text. We further calculated the total energies of the four magnetic states [NM, FM, antiferromagnetic 1 (AFM1), and antiferromagnetic 2 (AFM2)] in Fig. S3 [66]. The calculated results indicated that the total energy of the $1 \times 1 \times 2$ supercell for NM, AFM1, and AFM2 order was 645.9, 417.0, and 142.2 meV higher than that of the FM state, respectively. Thus the ferromagnetic state was identified as the ground state of $Rh_3Sn_2S_2$. To demonstrate the nontrivial band topology, the maximally localized Wannier functions (MLWFs) [72,73] were constructed (Fig. S5 [66]).

## III. RESULTS AND DISCUSSION

The shandite-type $Rh_3Sn_2S_2$ has a rhombohedral crystal structure with space group $R$-3$m$ (No. 166), in which Rh atoms are octahedrally coordinated by two S and four Sn atoms and form perfect kagome layers stacking along the $c$ axis [74] [Fig. 1(a)]. Although previous work suggests a magnetic instability [74], the magnetic ground state and the topological properties have not been uncovered for $Rh_3Sn_2S_2$. To figure out this issue, the experimental structure with $a = 5.6268$ Å and $c = 13.3067$ Å [74] is adopted to perform the DFT calculations. Our calculation results indicate that $Rh_3Sn_2S_2$ adopts a FM ground state and the partially filled Rh-$d$ orbital contributes 0.35 μB magnetic momentum (see Figs. S1– S4 [66]). Then, the Curie temperature is roughly estimated to be 61 K by $T_c \approx 2\Delta(E_{\mathrm{FM}} - E_{\mathrm{AFM2}})/3k_B$ within the MFT framework [56]. As shown in Figs. 1(c) and 1(d), the bands with spin polarization cross the $E_F$, suggesting a metallic character. One also notes that there are multiple band crossings in the spin-up channel (labeled by solid circles), while the valence and conduction bands are fully gapped in the spin-down state.

To further interpret the band characters, the irreducible representations (irreps) are obtained for the $R$-3$m$ space group [75]. As shown in Fig. 1(c), the intersections of bands Y1 and Y2, bands C1 and C2, and bands SM1 and SM2 form the doubly degenerate Weyl nodes along the $L$-$S$ (gray), Γ-$L$ (orange), and Γ-$W$ (green) paths, respectively. Besides, the eigenvalues of the mirror symmetry are opposite for the irreps Y1 and Y2, C1 and C2, and SM1 and SM2, respectively; that is, considering the mirror symmetry and the $C_{3z}$-rotation symmetry of space group $R$-3$m$ [76], six WNL-I's, six WNL-II's, and one WNL-III echoing the nodes labeled by orange, gray, and green in Fig. 1(c) would emerge in the BZ, respectively [see Figs. 2(a), 2(b), and 2(c)]. Moreover, the nontrivial topology of the WNLs can be evaluated by the Berry phase [77]

$$\gamma_n = \oint_C d\boldsymbol{R} \cdot A_n(\boldsymbol{R}), \tag{1}$$

where $C$ stands for a closed path encircling a generic point of the WNL and the vector $A_n(\boldsymbol{R})$ is the Berry connection. Remarkably, each WNL generates a Berry phase of $\pi$, suggesting that there are the nontrivial topological elements [77] in $Rh_3Sn_2S_2$. Besides, the nontrivial edge states corresponding to WNL-I, WNL-II, and WNL-III were obtained and are clearly displayed in Figs. 2(d), 2(e), and 2(f), respectively (see also Fig. S5 [66]).

Since Rh is a 4$d$ transition metal, the SOC contribution to the magnetic, electronic, and topological properties should be considered. The magnetocrystalline anisotropy energy (MAE) is first calculated to obtain the easy magnetization axis by varying the magnetic moment in the $xy$, $yz$, and $xz$ planes, respectively [Fig. 3(a)]. One notes that $Rh_3Sn_2S_2$ has a large

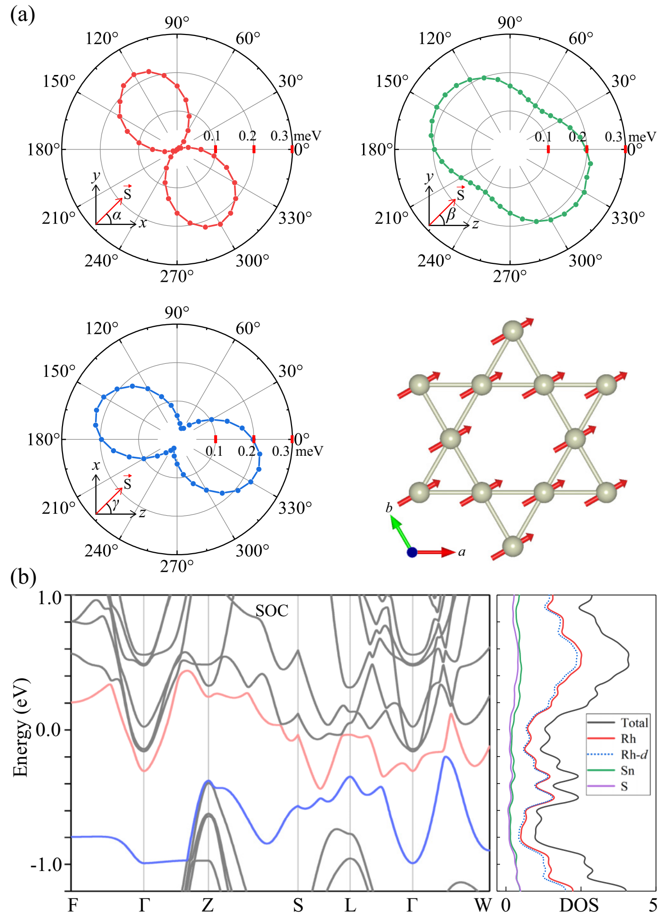


FIG. 3. Magnetic and electronic structure with SOC. (a) Angular dependence of the MAE and the canted magnetic order along the ($\sqrt{3}$ 1 0) direction. The included angles refer to the positive axis and are indicated by $\alpha$, $\beta$, and $\gamma$ in the top left, top right, and bottom left panels, respectively. The energy along the ($\sqrt{3}$ 1 0) direction is set as the reference point for the specific magnetization in the three planes. (b) The band structure (left panel) and the projected density of states (DOS; right panel) for the easy magnetization direction.

MAE up to 223 μeV/Rh atom and the energy of the $Rh_3Sn_2S_2$ unit cell is minimized when the magnetization lies in the $xy$ ($ab$) plane and forms a 30° angle to the $x$ ($a$) direction [Fig. 3(a)]. Then, this specific in-plane canted magnetic order with 0.35 μB for the Rh atom (see also Fig. S4 [66]) is employed for the subsequent calculations, and Fig. 3(b) illustrates the corresponding band structure. Noticeably, the band crossings in Fig. 1(c) vanish, and one can find that six chiral WPs with topological charge ±1 survive in WNL-I [Fig. 4(a)]. In view of the space inversion and the $C_{3z}$-rotation symmetry [47,76,78], one can map one WP to another, and hence these six WPs can be categorized as one pair.

We also note that these WPs are just 0.19 eV below the $E_F$ [Fig. 4(a)], and distinct phenomena in terms of the topological Fermi arc and AHE might be observed. Figure 4(b) displays a clear and long Fermi arc connecting the chiral WPs, which finding will be of benefit for the future experimental observations, such as angle-resolved photoemission spectroscopy (ARPES) measurements. Besides, the chiral negative and

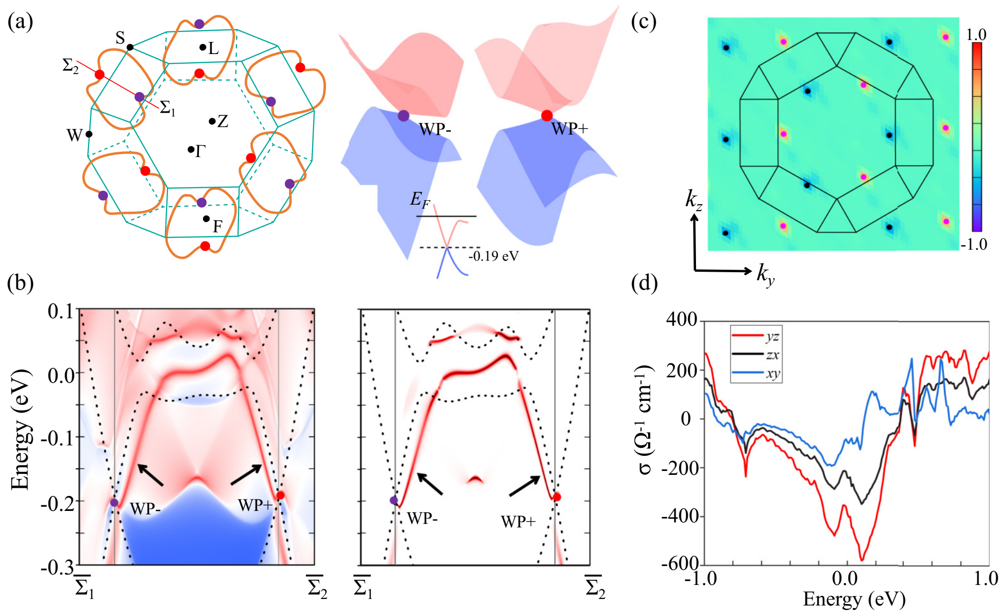


FIG. 4. Topological features, Berry curvature, and AHC with SOC. (a) The SOC breaks the WNLs and leaves WPs in WNL-I, which locate 0.19 eV below the $E_F$. The positions of WP+ and WP− are (−0.102, 0.247, −0.103) and (0.102, −0.247, 0.103), respectively. A cut from $\sum_1$ to $\sum_2$ connecting the Weyl nodes is displayed. (b) Calculated edge states with (left panel) and without (right panel) displaying the bulk states along the $\sum_1$ - $\sum_2$ path. The solid circles and black arrows highlight the band crossing points and the surface states, respectively. (c) Berry curvature distribution projected to the $k_y$-$k_z$ plane ($k_x = 0$). The Weyl nodes with opposite chirality are indicated by the magenta (+) and black (−) solid circles, respectively. The color bar is in arbitrary units. (d) The energy dependence of the AHC computed using WANNIER90 [72,73].

positive WPs, possessing the opposite topological charges of −1 (WP−) and +1 (WP+) [Fig. 4(a)], can act as a monopole source and sink of the Berry curvature (Fig. S6), respectively. Since the easy magnetization axis lies in the *ab* plane and is close to the *a* axis [Fig. 3(a)], it is convenient to calculate the Berry curvature $\Omega^x(\mathbf{k})$ that would be larger than the components $\Omega^y(\mathbf{k})$ and $\Omega^z(\mathbf{k})$ [25,79]. Significantly, Fig. 4(c) reveals that the hot spot of the integrated Berry curvature $\Omega^x(\mathbf{k})$ in the $k_x = 0$ plane corresponds to the distribution of the WPs, suggesting that the WPs boost the intrinsic Berry curvature [47,78]. Moreover, such a clean and large Berry curvature will produce an evident spin electron transport behavior, i.e., an intrinsic AHE. Then, the energy-dependent AHC $\sigma^x_{yz}$ can be acquired by integrating the Berry curvature of the occupied Bloch states based on the Kubo formula derivation [25,79]

$$\sigma^x_{yz}(E) = -\frac{e^2}{\hbar}\int_{\mathrm{BZ}}\frac{d^3k}{2\pi^3}\Omega^x_n(k), \tag{2}$$

$$\Omega^x_n(k) = \sum_{m\neq n}\frac{-2\,\mathrm{Im}\langle u_{nk}|\partial_y H(k)|u_{mk}\rangle\langle u_{mk}|\partial_z H(k)|u_{nk}\rangle}{[E_n(k)-E_m(k)]^2}. \tag{3}$$

The obtained AHC is displayed in Fig. 4(d), and $\sigma^x_{yz}$ reaches $-580\ \Omega^{-1}\,\mathrm{cm}^{-1}$, which is comparable to the large AHC of the kagome magnet $LiMn_6Sn_6$ (380 $\Omega^{-1}\,\mathrm{cm}^{-1}$) [45], $Mn_3Ge$ (500 $\Omega^{-1}\,\mathrm{cm}^{-1}$) [43], $Fe_3Sn_2$ (1100 $\Omega^{-1}\,\mathrm{cm}^{-1}$) [2], and $Co_3Sn_2S_2$ (1130 $\Omega^{-1}\,\mathrm{cm}^{-1}$) [47]. Similarly, the AHCs $\sigma^z_{xy}$ and $\sigma^y_{zx}$ are also calculated and displayed in Fig. 4(d), where $\sigma^z_{xy}$ and $\sigma^y_{zx}$ reach −192 and $-348\ \Omega^{-1}\,\mathrm{cm}^{-1}$, respectively, in the energy range of $E_F \pm 0.2$ eV, which values are comparable to those of the kagome magnets $Mn_3Sn$ (140 $\Omega^{-1}\,\mathrm{cm}^{-1}$) [22], $Mn_3Rh$ (284 $\Omega^{-1}\,\mathrm{cm}^{-1}$) [37], $Mn_3Ir$ (312 $\Omega^{-1}\,\mathrm{cm}^{-1}$) [37], $GdMn_6Sn_6$ (226 $\Omega^{-1}\,\mathrm{cm}^{-1}$) [44], $TbMn_6Sn_6$ (250 $\Omega^{-1}\,\mathrm{cm}^{-1}$) [40], and $YMn_6Sn_6$ (300 $\Omega^{-1}\,\mathrm{cm}^{-1}$) [38].

Now, we proceed with a brief discussion. The magnetic momentum of Rh (0.35 μB) is close to that in Heusler alloys $Rh_2MnAl$ (0.32 μB) and $Rh_2MnGa$ (0.31 μB) [80], suggesting that the calculated magnetic momentum is reasonable. Besides, the FM order is confirmed as the ground state of $Rh_3Sn_2S_2$, which is similar to the isostructural kagome ferromagnetic Weyl semimetal $Co_3Sn_2S_2$ [47]. Although $Rh_3Sn_2S_2$ and $Co_3Sn_2S_2$ adopt the same space group *R*-3*m*, they reveal diverse properties. First, the easy magnetization direction is in the *ab* plane for $Rh_3Sn_2S_2$ (Fig. 3), while $Co_3Sn_2S_2$ has an out-of-plane easy magnetization direction along the *c* axis [47]. Second, three sets of WNLs emerge for $Rh_3Sn_2S_2$ without considering SOC (Fig. 2), while there is only one set of WNLs for $Co_3Sn_2S_2$ [47]. Third, the main source of the Berry curvature is distributed in the vicinity of the WPs for $Rh_3Sn_2S_2$ (Fig. 4), while the WNLs dominate the contribution to the Berry curvature for $Co_3Sn_2S_2$ [47]. Besides, we should point out that the WPs in $Rh_3Sn_2S_2$ and $Co_3Sn_2S_2$ are protected by the same space inversion and $C_{3z}$-rotation symmetry [47,76,78], indicating that the AHE of $Rh_3Sn_2S_2$ might be tuned in an analogous way to $Co_3Sn_2S_2$, i.e., by strain [32], pressure [33,34], doping [39,42,81], and rotating the magnetization direction [82]. For simplicity, we rotate the magnetization direction to the *c* axis. Consequently, the AHCs $\sigma^z_{xy}$, $\sigma^x_{yz}$, and $\sigma^y_{zx}$ reach −616, −275, and $-170\ \Omega^{-1}\,\mathrm{cm}^{-1}$ around the Fermi level ($E_F \pm 0.2$ eV), respectively (Fig. S7 [66]), implying the presence of a tunable AHE in $Rh_3Sn_2S_2$ and the possible evolution of Weyl nodes from the magnetization alternation, similar to that reported in $Co_3Sn_2S_2$ [82] and the CrN monolayer [83]. Remarkably, the exotic transport features were found in $Co_3Sn_2S_2$ nanoflakes [54,55], and a high-Chern-number three-dimensional quantum AHE topological phase was proposed in $Co_3Sn_2S_2$ under tension [32], which will stimulate further research on undiscovered topological phenomena in $Co_3Sn_2S_2$ and $Rh_3Sn_2S_2$ and the potential applications in energy-efficient spintronics devices based on the AHE [84–86].

Noticeably, the AHE in kagome magnets and other systems [87–95] can be quantized in the magnetic WSMs with the broken TRS and the two-dimensional (2D) limit [96–98]. Following this scheme, one can realize the quantum anomalous Hall effect (QAHE) with nondissipative chiral edge states, which has promising applications in low-energy-consumption quantum devices [98]. For instance, the QAHE has been proposed in $HgCr_2Se_4$ [96], $Co_3Sn_2S_2$ [97,99], $Mn_3Sn$ [99], $Fe_3Sn_2$ [99], and $Mn_3(C_6O_6)_2$ [100], where the WPs are gapped through the breaking of periodic boundary conditions along one direction [97]. In other words, since the QAHE tends to emerge in 2D systems [98], layered magnetic WSMs are favored materials candidates [97]. Actually, the abovementioned intrinsic magnetic materials [96,97,99,100] all have the layered lattice structures, and most of them are layered kagome magnets [97,99,100]. As for $Rh_3Sn_2S_2$, Rh atoms construct the layered kagome lattice and contribute 0.35 μB magnetic moments; such lattice structure and magnetism are similar to those of $Co_3Sn_2S_2$ [47]. Moreover, the calculated MAE of $Rh_3Sn_2S_2$ is 0.223 meV/Rh atom, implying a moderate magnetic anisotropy that is comparable to that of those kagome magnets that are QAHE candidates [99,100]. In summary, $Rh_3Sn_2S_2$ possesses all the hallmarks of QAHE candidates, i.e., the layered lattice structure, the intrinsic WPs stemming from the broken TRS, the moderate magnetic anisotropy, and the tunable AHC, and we can infer that $Rh_3Sn_2S_2$ might be a promising material to obtain the QAHE phase in the extreme 2D limit [96–98].

## IV. CONCLUSION

$Rh_3Sn_2S_2$ is identified as a kagome ferromagnetic Weyl semimetal by DFT calculations. In the absence of SOC, $Rh_3Sn_2S_2$ exhibits three sets of nontrivial WNLs and clear topological surface states. Upon considering SOC, one of the WNLs transforms into WPs, and a distinct Fermi arc connects the WPs with opposite chirality. Then, the chiral WPs act as the monopole source and sink of the Berry curvature, yielding a large AHC around the Fermi level. These results demonstrate the nontrivial topological nature of $Rh_3Sn_2S_2$ and the influence of WPs on electron scattering. Overall, our findings highlight the magnetic, electronic, and topological properties as well as the tunable AHC of the kagome Weyl semimetal $Rh_3Sn_2S_2$, and this material provides a potential platform to realize the QAHE that has promising applications in energy-efficient spintronics devices.

## ACKNOWLEDGMENTS

This work was supported by the Natural Science Foundation of China (NSFC) with Grants No. 11704315, No. 12204074, and No. 12004272. D.-S.M. also acknowledges financial support from the China National Postdoctoral Program for Innovative Talent with Grant No. BX20220367. The computation work finished at Southwest University was supported by the high-performance-computing platform located in the School of Physical Science and Technology.

[1] M. R. Norman, Colloquium: Herbertsmithite and the search for the quantum spin liquid, Rev. Mod. Phys. **88**, 041002 (2016).

[2] L. Ye, M. Kang, J. Liu, F. Von Cube, C. R. Wicker, T. Suzuki, C. Jozwiak, A. Bostwick, E. Rotenberg, D. C. Bell, L. Fu, R. Comin, and J. G. Checkelsky, Massive Dirac fermions in a ferromagnetic kagome metal, Nature (London) **555**, 638 (2018).

[3] Z. Liu, M. Li, Q. Wang, G. Wang, C. Wen, K. Jiang, X. Lu, S. Yan, Y. Huang, D. Shen, J.-X. Yin, Z. Wang, Z. Yin, H. Lei, and S. Wang, Orbital-selective Dirac fermions and extremely flat bands in frustrated kagome-lattice metal CoSn, Nat. Commun. **11**, 4002 (2020).

[4] M. Li, Q. Wang, G. Wang, Z. Yuan, W. Song, R. Lou, Z. Liu, Y. Huang, Z. Liu, H. Lei, Z. Yin, and S. Wang, Dirac cone, flat band and saddle point in kagome magnet $YMn_6$ $Sn_6$, Nat. Commun. **12**, 3129 (2021).

[5] H. Chen, H. Yang, B. Hu, Z. Zhao, J. Yuan, Y. Xing, G. Qian, Z. Huang, G. Li, Y. Ye, S. Ma, S. Ni, H. Zhang, Q. Yin, C. Gong, Z. Tu, H. Lei, H. Tan, S. Zhou, C. Shen *et al.*, Roton pair density wave in a strong-coupling kagome superconductor, Nature (London) **599**, 222 (2021).

[6] M. Han, H. Inoue, S. Fang, C. John, L. Ye, M. K. Chan, D. Graf, T. Suzuki, M. P. Ghimire, W. J. Cho, E. Kaxiras, and J. G. Checkelsky, Evidence of two-dimensional flat band at the surface of antiferromagnetic kagome metal FeSn, Nat. Commun. **12**, 5345 (2021).

[7] Q. Wang, P. Kong, W. Shi, C. Pei, C. Wen, L. Gao, Y. Zhao, Q. Yin, Y. Wu, G. Li, H. Lei, J. Li, Y. Chen, S. Yan, and Y. Qi, Charge density wave orders and enhanced superconductivity under pressure in the kagome metal $CsV_3Sb_5$, Adv. Mater. **33**, 2102813 (2021).

[8] L. Nie, K. Sun, W. Ma, D. Song, L. Zheng, Z. Liang, P. Wu, F. Yu, J. Li, M. Shan, D. Zhao, S. Li, B. Kang, Z. Wu, Y. Zhou, K. Liu, Z. Xiang, Z. Ying, T. Wu, and X. Chen, Charge-density-wave-driven electronic nematicity in a kagome superconductor, Nature (London) **604**, 59 (2022).

[9] L. Zheng, Z. Wu, Y. Yang, L. Nie, M. Shan, K. Sun, D. Song, F. Yu, J. Li, D. Zhao, S. Li, B. Kang, Y. Zhou, K. Liu, Z. Xiang, J. Ying, Z. Wang, T. Wu, and X. Chen, Emergent charge order in pressurized kagome superconductor $CsV_3Sb_5$, Nature (London) **611**, 682 (2022).

[10] M. Shi, F. Yu, Y. Yang, F. Meng, B. Lei, Y. Luo, Z. Sun, J. He, R. Wang, Z. Jiang, Z. Liu, D. Shen, T. Wu, Z. Wang, Z. Xiang, J. Ying, and X. Chen, A new class of bilayer kagome lattice compounds with Dirac nodal lines and pressure-induced superconductivity, Nat. Commun. **13**, 2773 (2022).

[11] C. Mielke III, D. Das, J.-X. Yin, H. Liu, R. Gupta, Y.-X. Jiang, M. Medarde, X. Wu, H. C. Lei, J. Chang, P. Dai, Q. Si, H. Miao, R. Thomale, T. Neupert, Y. Shi, R. Khasanov, M. Hasan, H. Luetkens, and Z. Guguchia, Time-reversal symmetry-breaking charge order in a kagome superconductor, Nature (London) **602**, 245 (2022).

[12] M.-X. Wu, P. Wang, T. Yang, A.-L. Kuang, M.-Q. Kuang, and H.-K. Yuan, Possible topological states in two dimensional Kagome ferromagnet MnGe, J. Alloys Compd. **907**, 164389 (2022).

[13] M. Y. Jeong, H. J. Yang, H. S. Kim, Y. B. Kim, S. B. Lee, and M. J. Han, Crucial role of out-of-plane Sb *p* orbitals in Van Hove singularity formation and electronic correlations in the superconducting kagome metal $CsV_3Sb_5$, Phys. Rev. B **105**, 235145 (2022).

[14] M. Kang, S. Fang, J.-K. Kim, B. R. Ortiz, S. H. Ryu, J. Kim, J. Yoo, G. Sangiovanni, D. Di Sante, B.-G. Park, C. Jozwiak, A. Bostwick, E. Rotenberg, E. Kaxiras, S. D. Wilson, J.-H. Park, and R. Comin, Twofold van Hove singularity and origin of charge order in topological kagome superconductor $CsV_3Sb_5$, Nat. Phys. **18**, 301 (2022).

[15] H. W. S. Arachchige, W. R. Meier, M. Marshall, T. Matsuoka, R. Xue, M. A. McGuire, R. P. Hermann, H. Cao, and D. Mandrus, Charge density wave in kagome lattice intermetallic $ScV_6Sn_6$, Phys. Rev. Lett. **129**, 216402 (2022).

[16] J.-X. Yin, Y.-X. Jiang, X. Teng, M. S. Hossain, S. Mardanya, T.-R. Chang, Z. Ye, G. Xu, M. M. Denner, T. Neupert, B. Lienhard, H.-B. Deng, C. Setty, Q. Si, G. Chang, Z. Guguchia, B. Gao, N. Shumiya, Q. Zhang, T. A. Cochran *et al.*, Discovery of charge order and corresponding edge state in kagome magnet FeGe, Phys. Rev. Lett. **129**, 166401 (2022).

[17] Y. Zhong, J. Liu, X. Wu, Z. Guguchia, J.-X. Yin, A. Mine, Y. Li, S. Najafzadeh, D. Das, C. Mielke III, R. Khasanov, H. Luetkens, T. Suzuki, K. Liu, X. Han, T. Kondo, J. Hu, S. Shin, Z. Wang, X. Shi *et al.*, Nodeless electron pairing in $CsV_3$ $Sb_5$-derived kagome superconductors, Nature (London) **617**, 488 (2023).

[18] M. Kang, S. Fang, J. Yoo, B. R. Ortiz, Y. M. Oey, J. Choi, S. H. Ryu, J. Kim, C. Jozwiak, A. Bostwick, E. Rotenberg, E. Kaxiras, J. G. Checkelsky, S. D. Wilson, J.-H. Park, and R. Comin, Charge order landscape and competition with superconductivity in kagome metals, Nat. Mater. **22**, 186 (2023).

[19] Y. Luo, Y. Han, J. Liu, H. Chen, Z. Huang, L. Huai, H. Li, B. Wang, J. Shen, S. Ding, Z. Li, S. Peng, Z. Wei, Y. Miao, X. Sun, Z. Ou, Z. Xiang, M. Hashimoto, D. Lu, Y. Yao *et al.*, A unique van Hove singularity in kagome superconductor $CsV_{3-x}Ta_xSb_5$ with enhanced superconductivity, Nat. Commun. **14**, 3819 (2023).

[20] B. Liu, M.-Q. Kuang, Y. Luo, Y. Li, C. Hu, J. Liu, Q. Xiao, X. Zheng, L. Huai, S. Peng, Z. Wei, J. Shen, B. Wang, Y. Miao, X. Sun, Z. Ou, S. Cui, Z. Sun, M. Hashimoto, D. Lu *et al.*, Tunable Van Hove singularity without structural instability in kagome metal $CsTi_3Bi_5$, Phys. Rev. Lett. **131**, 026701 (2023).

[21] H. Chen, Q. Niu, and A. H. MacDonald, Anomalous Hall effect arising from noncollinear antiferromagnetism, Phys. Rev. Lett. **112**, 017205 (2014).

[22] S. Nakatsuji, N. Kiyohara, and T. Higo, Large anomalous Hall effect in a non-collinear antiferromagnet at room temperature, Nature (London) **527**, 212 (2015).

[23] T. Suzuki, R. Chisnell, A. Devarakonda, Y.-T. Liu, W. Feng, D. Xiao, J. W. Lynn, and J. Checkelsky, Large anomalous Hall effect in a half-Heusler antiferromagnet, Nat. Phys. **12**, 1119 (2016).

[24] H. Zhang, Y. L. Zhu, Y. Qiu, W. Tian, H. B. Cao, Z. Q. Mao, and X. Ke, Field-induced magnetic phase transitions and the resultant giant anomalous Hall effect in the antiferromagnetic half-Heusler compound DyPtBi, Phys. Rev. B **102**, 094424 (2020).

[25] N. Nagaosa, J. Sinova, S. Onoda, A. H. MacDonald, and N. P. Ong, Anomalous Hall effect, Rev. Mod. Phys. **82**, 1539 (2010).

[26] S.-Y. Yang, Y. Wang, B. R. Ortiz, D. Liu, J. Gayles, E. Derunova, R. Gonzalez-Hernandez, L. Šmejkal, Y. Chen, S. S. Parkin, S. D. Wilson, E. S. Toberer, T. McQueen, and M. N. Ali, Giant, unconventional anomalous Hall effect in the metallic frustrated magnet candidate, $KV_3Sb_5$, Sci. Adv. **6**, eabb6003 (2020).

[27] Y. Fujishiro, N. Kanazawa, R. Kurihara, H. Ishizuka, T. Hori, F. S. Yasin, X. Yu, A. Tsukazaki, M. Ichikawa, M. Kawasaki, N. Nagaosa, M. Tokunaga, and Y. Tokura, Giant anomalous Hall effect from spin-chirality scattering in a chiral magnet, Nat. Commun. **12**, 317 (2021).

[28] M. Uchida, S. Sato, H. Ishizuka, R. Kurihara, T. Nakajima, Y. Nakazawa, M. Ohno, M. Kriener, A. Miyake, K. Ohishi, T. Morikawa, S. M. Bahramy, T.-H. Arima, M. Tokunaga, N. Nagaosa, and M. Kawasaki, Above-ordering-temperature large anomalous Hall effect in a triangular-lattice magnetic semiconductor, Sci. Adv. **7**, eabl5381 (2021).

[29] Y. Liu, C.-C. Liu, Q.-Q. Zhu, L.-W. Ji, S.-Q. Wu, Y.-L. Sun, J.-K. Bao, W.-H. Jiao, X.-F. Xu, Z. Ren, and G.-H. Cao, Enhancement of superconductivity and suppression of charge-density wave in As-doped $CsV_3Sb_5$, Phys. Rev. Mater. **6**, 124803 (2022).

[30] G. Zheng, C. Tan, Z. Chen, M. Wang, X. Zhu, S. Albarakati, M. Algarni, J. Partridge, L. Farrar, J. Zhou, W. Ning, M. Tian, M. S. Fuhrer, and L. Wang, Electrically controlled superconductor-to-failed insulator transition and giant anomalous Hall effect in kagome metal $CsV_3Sb_5$ nanoflakes, Nat. Commun. **14**, 678 (2023).

[31] D. Torres-Amaris, A. Bautista-Hernandez, R. González-Hernández, A. H. Romero, and A. C. Garcia-Castro, Anomalous Hall conductivity control in $Mn_3NiN$ antiperovskite by epitaxial strain along the kagome plane, Phys. Rev. B **106**, 195113 (2022).

[32] H. Sun and Q. Liu, Boosting the intrinsic anomalous Hall effect through a topological phase transition in the magnetic Weyl semimetal $Co_3Sn_2S_2$, Phys. Rev. B **107**, 205138 (2023).

[33] X. Chen, M. Wang, C. Gu, S. Wang, Y. Zhou, C. An, Y. Zhou, B. Zhang, C. Chen, Y. Yuan, M. Qi, L. Zhang, H. Zhou, J. Zhou, Y. Yao, and Z. Yang, Pressure-tunable large anomalous Hall effect of the ferromagnetic kagome-lattice Weyl semimetal $Co_3Sn_2S_2$, Phys. Rev. B **100**, 165145 (2019).

[34] Z. Y. Liu, T. Zhang, S. X. Xu, P. T. Yang, Q. Wang, H. C. Lei, Y. Sui, Y. Uwatoko, B. S. Wang, H. M. Weng, J. P. Sun, and J.-G. Cheng, Pressure effect on the anomalous Hall effect of ferromagnetic Weyl semimetal $Co_3Sn_2S_2$, Phys. Rev. Mater. **4**, 044203 (2020).

[35] T. Asaba, Y. Su, M. Janoschek, J. D. Thompson, S. M. Thomas, E. D. Bauer, S.-Z. Lin, and F. Ronning, Large

tunable anomalous Hall effect in the kagome antiferromagnet $U_3Ru_4Al_{12}$, Phys. Rev. B **102**, 035127 (2020).

[36] Z. Guguchia, J. Verezhak, D. Gawryluk, S. Tsirkin, J.-X. Yin, I. Belopolski, H. Zhou, G. Simutis, S.-S. Zhang, T. Cochran, G. Chang, E. Pomjakushina, L. Keller, Z. Skrzeczkowska, Q. Wang, C. Lei, R. Khasanov, A. Amato, S. Jia, T. Neupert *et al.*, Tunable anomalous Hall conductivity through volume-wise magnetic competition in a topological kagome magnet, Nat. Commun. **11**, 559 (2020).

[37] Y. Zhang, Y. Sun, H. Yang, J. Železný, S. P. P. Parkin, C. Felser, and B. Yan, Strong anisotropic anomalous Hall effect and spin Hall effect in the chiral antiferromagnetic compounds $Mn_3X$ ($X$ = Ge, Sn, Ga, Ir, Rh, and Pt), Phys. Rev. B **95**, 075128 (2017).

[38] C. Q. Xu, T. W. Heitmann, H. Zhang, X. Xu, and X. Ke, Magnetic phase transition, magnetoresistance, and anomalous Hall effect in Ga-substituted $YMn_6Sn_6$ with a ferromagnetic kagome lattice, Phys. Rev. B **104**, 024413 (2021).

[39] Z. Zhang, J.-Y. You, X.-Y. Ma, B. Gu, and G. Su, Kagome quantum anomalous Hall effect with high Chern number and large band gap, Phys. Rev. B **103**, 014410 (2021).

[40] L. Gao, S. Shen, Q. Wang, W. Shi, Y. Zhao, C. Li, W. Cao, C. Pei, J.-Y. Ge, G. Li, J. Li, Y. Chen, S. Yan, and Y. Qi, Anomalous Hall effect in ferrimagnetic metal $RMn_6Sn_6$ (R = Tb, Dy, Ho) with clean Mn kagome lattice, Appl. Phys. Lett. **119**, 092405 (2021).

[41] W. Ma, X. Xu, J.-X. Yin, H. Yang, H. Zhou, Z.-J. Cheng, Y. Huang, Z. Qu, F. Wang, M. Z. Hasan, and S. Jia, Rare earth engineering in $RMn_6Sn_6$ ($R$ = Gd–Tm, Lu) topological kagome magnets, Phys. Rev. Lett. **126**, 246602 (2021).

[42] W. Luo, Y. Nakamura, J. Park, and M. Yoon, Cobalt-based magnetic Weyl semimetals with high-thermodynamic stabilities, npj Comput. Mater. **7**, 2 (2021).

[43] A. K. Nayak, J. E. Fischer, Y. Sun, B. Yan, J. Karel, A. C. Komarek, C. Shekhar, N. Kumar, W. Schnelle, J. Kübler, C. Felser, and S. S. P. Parkin, Large anomalous Hall effect driven by a nonvanishing Berry curvature in the noncolinear antiferromagnet $Mn_3Ge$, Sci. Adv. **2**, e1501870 (2016).

[44] T. Asaba, S. M. Thomas, M. Curtis, J. D. Thompson, E. D. Bauer, and F. Ronning, Anomalous Hall effect in the kagome ferrimagnet $GdMn_6Sn_6$, Phys. Rev. B **101**, 174415 (2020).

[45] D. Chen, C. Le, C. Fu, H. Lin, W. Schnelle, Y. Sun, and C. Felser, Large anomalous Hall effect in the kagome ferromagnet $LiMn_6Sn_6$, Phys. Rev. B **103**, 144410 (2021).

[46] X. Zhou, W. Feng, Y. Li, and Y. Yao, Spin-chirality-driven quantum anomalous and quantum topological Hall effects in chiral magnets, Nano Lett. **23**, 5680 (2023).

[47] E. Liu, Y. Sun, N. Kumar, L. Muechler, A. Sun, L. Jiao, S.-Y. Yang, D. Liu, A. Liang, Q. Xu, J. Kroder, V. Süß, H. Borrmann, C. Shekhar, Z. Wang, C. Xi, W. Wang, W. Schnelle, S. Wirth, Y. Chen *et al.*, Giant anomalous Hall effect in a ferromagnetic kagome-lattice semimetal, Nat. Phys. **14**, 1125 (2018).

[48] Q. Wang, Y. Xu, R. Lou, Z. Liu, M. Li, Y. Huang, D. Shen, H. Weng, S. Wang, and H. Lei, Large intrinsic anomalous Hall effect in half-metallic ferromagnet $Co_3Sn_2S_2$ with magnetic Weyl fermions, Nat. Commun. **9**, 3681 (2018).

[49] T. Tomizawa and H. Kontani, Anomalous Hall effect in the $t_{2g}$ orbital kagome lattice due to noncollinearity: Significance of the orbital Aharonov-Bohm effect, Phys. Rev. B **80**, 100401(R) (2009).

[50] X. Wang and J. Tan, Intrinsic anomalous Hall effect and Lifshitz transition in a ferromagnetic kagome-lattice metal, Appl. Phys. Lett. **121**, 161903 (2022).

[51] E. Rosenberg, J. M. DeStefano, Y. Guo, J. S. Oh, M. Hashimoto, D. Lu, R. J. Birgeneau, Y. Lee, L. Ke, M. Yi, and J.-H. Chu, Uniaxial ferromagnetism in the kagome metal $TbV_6Sn_6$, Phys. Rev. B **106**, 115139 (2022).

[52] H. Zhou, M. Shi, Y. Huang, W. Ma, X. Xu, J. Wang, and S. Jia, Metamagnetic transition and anomalous Hall effect in Mn-based kagomé magnets $RMn_6$ $Ge_6$ ($R$ = Tb–Lu), Phys. Rev. Mater. **7**, 024404 (2023).

[53] G. Dhakal, F. C. Kabeer, A. K. Pathak, F. Kabir, N. Poudel, R. Filippone, J. Casey, A. P. Sakhya, S. Regmi, C. Sims, K. Dimitri, P. Manfrinetti, K. Gofryk, P. M. Oppeneer, and M. Neupane, Anisotropically large anomalous and topological Hall effect in a kagome magnet, Phys. Rev. B **104**, L161115 (2021).

[54] S.-Y. Yang, J. Noky, J. Gayles, F. K. Dejene, Y. Sun, M. Dorr, Y. Skourski, C. Felser, M. N. Ali, E. Liu, and S. S. P. Parkin, Field-modulated anomalous Hall conductivity and planar Hall effect in $Co_3Sn_2S_2$ nanoflakes, Nano Lett. **20**, 7860 (2020).

[55] M. Tanaka, Y. Fujishiro, M. Mogi, Y. Kaneko, T. Yokosawa, N. Kanazawa, S. Minami, T. Koretsune, R. Arita, S. Tarucha, M. Yamamoto, and Y. Tokura, Topological kagome magnet $Co_3Sn_2S_2$ thin flakes with high electron mobility and large anomalous Hall effect, Nano Lett. **20**, 7476 (2020).

[56] X. Jiang, Q. Liu, J. Xing, N. Liu, Y. Guo, Z. Liu, and J. Zhao, Recent progress on 2D magnets: Fundamental mechanism, structural design and modification, Appl. Phys. Rev. **8**, 031305 (2021).

[57] G. Kresse and J. Hafner, *Ab initio* molecular-dynamics simulation of the liquid-metal-amorphous-semiconductor transition in germanium, Phys. Rev. B **49**, 14251 (1994).

[58] G. Kresse and J. Furthmüller, Efficient iterative schemes for *ab initio* total-energy calculations using a plane-wave basis set, Phys. Rev. B **54**, 11169 (1996).

[59] J. P. Perdew, K. Burke, and M. Ernzerhof, Generalized gradient approximation made simple, Phys. Rev. Lett. **77**, 3865 (1996).

[60] J. Sun, A. Ruzsinszky, and J. P. Perdew, Strongly constrained and appropriately normed semilocal density functional, Phys. Rev. Lett. **115**, 036402 (2015).

[61] R. Schaffer, E. K.-H. Lee, B.-J. Yang, and Y. B. Kim, Recent progress on correlated electron systems with strong spin-orbit coupling, Rep. Prog. Phys. **79**, 094504 (2016).

[62] J. Heyd, G. E. Scuseria, and M. Ernzerhof, Hybrid functionals based on a screened Coulomb potential, J. Chem. Phys. **118**, 8207 (2003).

[63] J. Heyd and G. E. Scuseria, Efficient hybrid density functional calculations in solids: Assessment of the Heyd-Scuseria-Ernzerhof screened Coulomb hybrid functional, J. Chem. Phys. **121**, 1187 (2004).

[64] Q. Wu, S. Zhang, H.-F. Song, M. Troyer, and A. A. Soluyanov, Wanniertools: An open-source software package for novel topological materials, Comput. Phys. Commun. **224**, 405 (2018).

[65] M. Ernzerhof and G. E. Scuseria, Assessment of the Perdew-Burke-Ernzerhof exchange-correlation functional, J. Chem. Phys. **110**, 5029 (1999).

[66] See Supplemental Material at http://link.aps.org/supplemental/10.1103/PhysRevB.108.174430 for the band structure and projected density of states (PDOS) of $Rh_3Sn_2S_2$; a sketch map of the NM, FM, AFM1, and AFM2 orders; the Berry curvature of WP$\pm$; and the AHC of $Rh_3Sn_2S_2$ when the magnetization is along the (001) direction.

[67] C. Wu, D. Bergman, L. Balents, and S. Das Sarma, Flat bands and Wigner crystallization in the honeycomb optical lattice, Phys. Rev. Lett. **99**, 070401 (2007).

[68] E. Tang, J.-W. Mei, and X.-G. Wen, High-temperature fractional quantum Hall states, Phys. Rev. Lett. **106**, 236802 (2011).

[69] C. Franchini, R. Kováčik, M. Marsman, S. S. Murthy, J. He, C. Ederer, and G. Kresse, Maximally localized Wannier functions in $LaMnO_3$ within PBE $+U$, hybrid functionals and partially self-consistent GW: an efficient route to construct *ab initio* tight-binding parameters for $e_g$ perovskites, J. Phys.: Condens. Matter **24**, 235602 (2012).

[70] W. Setyawan, R. M. Gaume, S. Lam, R. S. Feigelson, and S. Curtarolo, High-throughput combinatorial database of electronic band structures for inorganic scintillator materials, ACS Comb. Sci. **13**, 382 (2011).

[71] O. Y. Long, G. S. Gautam, and E. A. Carter, Evaluating optimal $U$ for $3d$ transition-metal oxides within the SCAN+$U$ framework, Phys. Rev. Mater. **4**, 045401 (2020).

[72] A. A. Mostofi, J. R. Yates, Y.-S. Lee, I. Souza, D. Vanderbilt, and N. Marzari, wannier90: A tool for obtaining maximally-localised Wannier functions, Comput. Phys. Commun. **178**, 685 (2008).

[73] A. A. Mostofi, J. R. Yates, G. Pizzi, Y.-S. Lee, I. Souza, D. Vanderbilt, and N. Marzari, An updated version of wannier90: A tool for obtaining maximally-localised Wannier functions, Comput. Phys. Commun. **185**, 2309 (2014).

[74] I. Anusca, A. Schmid, P. Peter, J. Rothballer, F. Pielnhofer, and R. Weihrich, Half antiperovskites: IV. Crystallographic and electronic structure investigations on $A_2Rh_3S_2$ ($A$ = In, Sn, Tl, Pb, Bi), Z. Anorg. Allg. Chem. **635**, 2410 (2009).

[75] J. Gao, Q. Wu, C. Persson, and Z. Wang, Irvsp: To obtain irreducible representations of electronic states in the VASP, Comput. Phys. Commun. **261**, 107760 (2021).

[76] Z.-M. Yu, Z. Zhang, G.-B. Liu, W. Wu, X.-P. Li, R.-W. Zhang, S. A. Yang, and Y. Yao, Encyclopedia of emergent particles in three-dimensional crystals, Sci. Bull. **67**, 375 (2022).

[77] D. Xiao, M.-C. Chang, and Q. Niu, Berry phase effects on electronic properties, Rev. Mod. Phys. **82**, 1959 (2010).

[78] K. Yang, P. Willke, Y. Bae, A. Ferrón, J. L. Lado, A. Ardavan, J. Fernández-Rossier, A. J. Heinrich, and C. P. Lutz, Electrically controlled nuclear polarization of individual atoms, Nat. Phys. **13**, 1120 (2018).

[79] Y. Yao, L. Kleinman, A. H. MacDonald, J. Sinova, T. Jungwirth, D. S. Wang, E. Wang, and Q. Niu, First principles calculation of anomalous Hall conductivity in ferromagnetic bcc Fe, Phys. Rev. Lett. **92**, 037204 (2004).

[80] J. Noky, Y. Zhang, J. Gooth, C. Felser, and Y. Sun, Giant anomalous Hall and Nernst effect in magnetic cubic Heusler compounds, npj Comput. Mater. **6**, 77 (2020).

[81] G. S. Thakur, P. Vir, S. N. Guin, C. Shekhar, R. Weihrich, Y. Sun, N. Kumar, and C. Felser, Intrinsic anomalous Hall effect in Ni-substituted magnetic Weyl semimetal $Co_3Sn_2S_2$, Chem. Mater. **32**, 1612 (2020).

[82] M. P. Ghimire, J. I. Facio, J.-S. You, L. Ye, J. G. Checkelsky, S. Fang, E. Kaxiras, M. Richter, and J. van den Brink, Creating Weyl nodes and controlling their energy by magnetization rotation, Phys. Rev. Res. **1**, 032044(R) (2019).

[83] T. He, X. Zhang, Y. Liu, X. Dai, G. Liu, Z.-M. Yu, and Y. Yao, Ferromagnetic hybrid nodal loop and switchable type-I and type-II Weyl fermions in two dimensions, Phys. Rev. B **102**, 075133 (2020).

[84] M. DC, R. Grassi, J.-Y. Chen, M. Jamali, D. Reifsnyder Hickey, D. Zhang, Z. Zhao, H. Li, P. Quarterman, Y. Lv, M. Li, A. Manchon, K. A. Mkhoyan, T. Low, and J.-P. Wang, Room-temperature high spin–orbit torque due to quantum confinement in sputtered $Bi_xSe_{(1-x)}$ films, Nat. Mater. **17**, 800 (2018).

[85] S. Iihama, T. Taniguchi, K. Yakushiji, A. Fukushima, Y. Shiota, S. Tsunegi, R. Hiramatsu, S. Yuasa, Y. Suzuki, and H. Kubota, Spin-transfer torque induced by the spin anomalous Hall effect, Nat. Electron. **1**, 120 (2018).

[86] J. Puebla, J. Kim, K. Kondou, and Y. Otani, Spintronic devices for energy-efficient data storage and energy harvesting, Commun. Mater. **1**, 24 (2020).

[87] H. Kontani, T. Tanaka, D. S. Hirashima, K. Yamada, and J. Inoue, Giant orbital Hall effect in transition metals: Origin of large spin and anomalous Hall effects, Phys. Rev. Lett. **102**, 016601 (2009).

[88] H. Chen, Z. Feng, H. Yan, P. Qin, X. Zhou, H. Guo, X. Wang, H. Wu, X. Zhang, Z. Meng, and Z. Liu, Anomalous Hall effect in antiferromagnetic Cr thin films, Phys. Rev. B **104**, 064428 (2021).

[89] Y. Shiomi, Y. Handa, T. Kikkawa, and E. Saitoh, Anomalous Hall effect with giant hysteresis loop in $La_{0.67}Sr_{0.33}MnO_3|SrRuO_3$ superlattices, Phys. Rev. B **92**, 024418 (2015).

[90] Y. Wang, T. F. Rosenbaum, D. Prabhakaran, A. T. Boothroyd, and Y. Feng, Approaching the quantum critical point in a highly correlated all-in–all-out antiferromagnet, Phys. Rev. B **101**, 220404(R) (2020).

[91] T. Jungwirth, Q. Niu, and A. H. MacDonald, Anomalous Hall effect in ferromagnetic semiconductors, Phys. Rev. Lett. **88**, 207208 (2002).

[92] P. Li, J. Koo, W. Ning, J. Li, L. Miao, L. Min, Y. Zhu, Y. Wang, N. Alem, C.-X. Liu, Z. Mao, and B. Yan, Giant room temperature anomalous Hall effect and tunable topology in a ferromagnetic topological semimetal $Co_2MnAl$, Nat. Commun. **11**, 3476 (2020).

[93] X. Zhang, S. Sun, and H. Lei, Massive fermions with low mobility in antiferromagnet orthorhombic CuMnAs single crystals, Phys. Rev. B **96**, 235105 (2017).

[94] H. Sakai, H. Fujimura, S. Sakuragi, M. Ochi, R. Kurihara, A. Miyake, M. Tokunaga, T. Kojima, D. Hashizume, T. Muro, K. Kuroda, T. Kondo, T. Kida, M. Hagiwara, K. Kuroki, M. Kondo, K. Tsuruda, H. Murakawa, and N. Hanasaki, Bulk

quantum Hall effect of spin-valley coupled Dirac fermions in the polar antiferromagnet $BaMnSb_2$, Phys. Rev. B **101**, 081104(R) (2020).

[95] B. H. Rimmler, B. K. Hazra, B. Pal, K. Mohseni, J. M. Taylor, A. Bedoya-Pinto, H. Deniz, M. Tangi, I. Kostanovskiy, C. Luo, R. R. Neumann, A. Ernst, F. Radu, I. Mertig, H. L. Meyerheim, and S. S. P. Parkin, Atomic displacements enabling the observation of the anomalous Hall effect in a non-collinear antiferromagnet, Adv. Mater. **35**, 2209616 (2023).

[96] G. Xu, H. Weng, Z. Wang, X. Dai, and Z. Fang, Chern semimetal and the quantized anomalous Hall effect in $HgCr_2Se_4$, Phys. Rev. Lett. **107**, 186806 (2011).

[97] L. Muechler, E. Liu, J. Gayles, Q. Xu, C. Felser, and Y. Sun, Emerging chiral edge states from the confinement of a magnetic Weyl semimetal in $Co_3Sn_2S_2$, Phys. Rev. B **101**, 115106 (2020).

[98] C.-Z. Chang, C.-X. Liu, and A. H. MacDonald, Colloquium: Quantum anomalous Hall effect, Rev. Mod. Phys. **95**, 011002 (2023).

[99] K. Kobayashi, M. Takagaki, and K. Nomura, Robust magnetotransport in disordered ferromagnetic kagome layers with quantum anomalous Hall effect, Phys. Rev. B **100**, 161301(R) (2019).

[100] X. Zhang, Y. Li, T. He, M. Zhao, L. Jin, C. Liu, X. Dai, Y. Liu, H. Yuan, and G. Liu, Time-reversal symmetry breaking Weyl semimetal and tunable quantum anomalous Hall effect in a two-dimensional metal-organic framework, Phys. Rev. B **108**, 054404 (2023).